









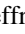




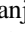

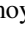

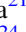













# SCEXAO/CHARIS High-contrast Imaging of Spirals and Darkening Features in the HD 34700 A Protoplanetary Disk

Taichi Uyama<sup>1,2,3</sup> , Thayne Currie<sup>4,5,6</sup> , Valentin Christiaens<sup>7</sup> , Jaehan Bae<sup>8,28</sup> , Takayuki Muto<sup>9</sup>,  
Sanemichi Z. Takahashi<sup>3</sup> , Ryo Tazaki<sup>9</sup> , Marie Ygouf<sup>1</sup> , Jeremy N. Kasdin<sup>10</sup> , Tyler Groff<sup>11</sup> , Timothy D. Brandt<sup>12</sup> ,  
Jeffrey Chilcote<sup>13</sup> , Masahiko Hayashi<sup>3</sup> , Michael W. McElwain<sup>14</sup> , Olivier Guyon<sup>5,15,16</sup> , Julien Lozi<sup>5</sup> ,  
Nemanja Jovanovic<sup>17</sup> , Frantz Martinache<sup>18</sup> , Tomoyuki Kudo<sup>5</sup> , Motohide Tamura<sup>3,19,20</sup> , Eiji Akiyama<sup>21</sup> ,  
Charles A. Beichman<sup>1,2</sup> , Carol A. Grady<sup>6,14,22</sup> , Gillian R. Knapp<sup>23</sup> , Jungmi Kwon<sup>19</sup> , Michael Sitko<sup>24</sup> ,  
Michihiro Takami<sup>25</sup> , Kevin R. Wagner<sup>15,26</sup> , John P. Wisniewski<sup>27</sup> , and Yi Yang<sup>3,19</sup> 

<sup>1</sup>Infrared Processing and Analysis Center, California Institute of Technology, Pasadena, CA 91125, USA

<sup>2</sup>NASA Exoplanet Science Institute, Pasadena, CA 91125, USA

<sup>3</sup>National Astronomical Observatory of Japan, 2-21-1 Osawa, Mitaka, Tokyo 181-8588, Japan

<sup>4</sup>NASA-Ames Research Center, Moffett Blvd., Moffett Field, CA 94035, USA

<sup>5</sup>Subaru Telescope, National Astronomical Observatory of Japan, National Institutes of Natural Sciences, 650 North A'ohōkū Place, Hilo, HI 96720, USA

<sup>6</sup>Eureka Scientific, 2452 Delmer, Suite 100, Oakland, CA 96002, USA

<sup>7</sup>School of Physics and Astronomy, Monash University, 10 College Walk, Clayton, Melbourne 3800, Vic, Australia

<sup>8</sup>Earth and Planets Laboratory, Carnegie Institution for Science, 5241 Broad Branch Road NW, Washington, DC 20015, USA

<sup>9</sup>Division of Liberal Arts, Kogakuin University 2665-1, Nakano-cho, Hachioji-chi, Tokyo, 192-0015, Japan

<sup>10</sup>Department of Mechanical Engineering, Princeton University, Princeton, NJ 08544, USA

<sup>11</sup>NASA-Goddard Space Flight Center, Greenbelt, MD 20771, USA

<sup>12</sup>Department of Physics, University of California-Santa Barbara, Santa Barbara, CA 93106, USA

<sup>13</sup>Department of Physics, University of Notre Dame, 225 Nieuwland Science Hall, Notre Dame, IN 46556, USA

<sup>14</sup>Exoplanets and Stellar Astrophysics Laboratory, Code 667, Goddard Space Flight Center, Greenbelt, MD 20771, USA

<sup>15</sup>Steward Observatory, University of Arizona, Tucson, AZ 85721, USA

<sup>16</sup>Astrobiology Center, National Institutes of Natural Sciences, 2-21-1 Osawa, Mitaka, Tokyo, Japan

<sup>17</sup>Department of Astronomy, California Institute of Technology, 1200 E. California Blvd., Pasadena, CA 91125, USA

<sup>18</sup>Université Côte d'Azur, Observatoire de la Côte d'Azur, CNRS, Laboratoire Lagrange, France

<sup>19</sup>Department of Astronomy, The University of Tokyo, 7-3-1, Hongo, Bunkyo-ku, Tokyo 113-0033, Japan

<sup>20</sup>Astrobiology Center of NINS, 2-21-1 Osawa, Mitaka, Tokyo 181-8588, Japan

<sup>21</sup>Department of Engineering, Niigata Institute of Technology, 1719 Fujihashi, Kashiwazaki, Niigata 945-1195, Japan

<sup>22</sup>Goddard Center for Astrobiology, 8800 Greenbelt Road, Greenbelt, MD 20771, USA

<sup>23</sup>Department of Astrophysical Science, Princeton University, Peyton Hall, Ivy Lane, Princeton, NJ 08544, USA

<sup>24</sup>Space Science Institute, 4765 Walnut St, Suite B, Boulder, CO 80301, USA

<sup>25</sup>Institute of Astronomy and Astrophysics, Academia Sinica, National Taiwan University, No.1, Sec. 4, Roosevelt Rd, Taipei 10617, Taiwan, R.O.C.

<sup>26</sup>NASA NExSS Earths in Other Solar Systems Team, USA

<sup>27</sup>Homer L. Dodge Department of Physics and Astronomy, University of Oklahoma, 440 W. Brooks Street, Norman, OK 73019, USA

Received 2020 June 1; revised 2020 July 22; accepted 2020 July 22; published 2020 September 9

## Abstract

We present Subaru/SCEXAO+Coronagraphic High Angular Resolution Imaging Spectrograph (CHARIS) broadband (*JHK*-band) integral field spectroscopy of HD 34700 A. CHARIS data recover HD 34700 A's disk ring and confirm multiple spirals discovered by Monnier et al. We set limits on substellar companions of  $\sim 12 M_{\text{Jup}}$  at  $0''.3$  (in the ring gap) and  $\sim 5 M_{\text{Jup}}$  at  $0''.75$  (outside the ring). The data reveal darkening effects on the ring and spiral, although we do not identify the origin of each feature such as shadows or physical features related to the outer spirals. Geometric albedos converted from the surface brightness suggest a greater scale height and/or prominently abundant submicron dust at position angles between  $\sim 45^\circ$  and  $90^\circ$ . Spiral fitting resulted in very large pitch angles ( $\sim 30^\circ$ – $50^\circ$ ); a stellar flyby of HD 34700 B or infall from a possible envelope is perhaps a reasonable scenario to explain the large pitch angles.

*Unified Astronomy Thesaurus concepts:* [Protoplanetary disks \(1300\)](#); [Coronagraphic imaging \(313\)](#)

## 1. Introduction

Protoplanetary disks around young ( $\lesssim 10$  Myr) stars are key laboratories for exploring planet formation. Recent high angular resolution observations of these disks in scattered light through thermal emission in the submillimeter region reveal a variety of asymmetric features—e.g., gaps, rings, and spirals—that may be traced to planet formation processes (e.g., Andrews et al. 2018; Avenhaus et al. 2018). Theoretical studies have predicted that some such asymmetric features are related to planet formation (e.g., Dodson-Robinson & Salyk 2011;

Zhu et al. 2011) and recently Very Large Telescope (VLT) and MagAO high-contrast imaging observations led to reports of the first convincing protoplanets within a gap of PDS 70's protoplanetary disk (Keppler et al. 2018; Wagner et al. 2018; Haffert et al. 2019). High-contrast imaging opened a new window for investigating planet formation mechanisms but the occurrence rate of detected young planets is much smaller ( $\sim 1\%$ – $3\%$  at 10–300 au; e.g., Bowler 2016; Nielsen et al. 2019) than the occurrence rate of asymmetric disks that are favorable for planet formation (e.g., Dong et al. 2018a).

Recently HD 34700 A became one of the most intriguing young systems with a large gap and multiple spirals in its disk (Monnier et al. 2019). Previously HD 34700 A was known to

<sup>28</sup> NHFP Sagan Fellow.

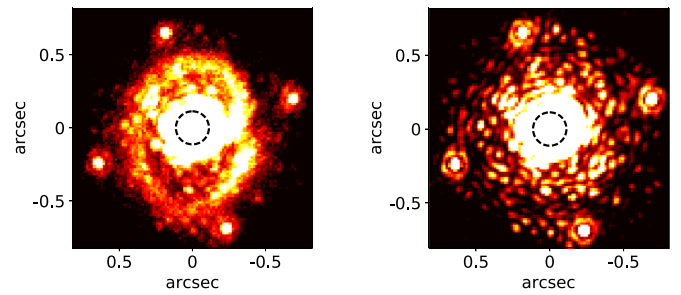
be a binary (HD 34700 Aab) with a significant far-infrared excess that had been regarded as a debris disk ( $\gtrsim 10$  Myr; Torres 2004). This system has two other companions (HD 34700 BC) located at  $\sim 5''.2$  and  $\sim 9''.2$  respectively (Sterzik et al. 2005). A precise measurement of the parallax with Gaia ( $356.5_{-6.0}^{+6.3}$  pc) showed a larger distance than the previous assumption, which made one infer a younger age. Monnier et al. (2019) implemented radiative transfer modeling along with Gemini/GPI *JH*-band observations and proved that HD 34700 A is a young system ( $\sim 5$  Myr) surrounded by a protoplanetary disk. Although their model showed good agreement with polarimetric data in the *J* band, it had some differences between GPI-based *JH*-band total intensity and *H*-band polarized intensity. Another intriguing feature in the HD 34700 A disk is its spiral features: previous high angular resolution observations have indicated a variety of morphology in disks at various evolutionary stages (e.g., AB Aur, SAO 206462, MWC 758, HD 100453, HD 100546, HD 142527, Elias 2-27, CQ Tau, GG Tau; Hashimoto et al. 2011; Muto et al. 2012; Grady et al. 2013; Avenhaus et al. 2014; Currie et al. 2015; Wagner et al. 2015; Pérez et al. 2016; Keppler et al. 2020; Uyama et al. 2020). Among these disks this object has the largest number of spirals in a disk, the mechanism for which is still unclear.

In this study we present integral field spectroscopy (IFS) observations of HD 34700 A taken with the Coronagraphic High Angular Resolution Imaging Spectrograph (CHARIS) and the Subaru Coronagraphic Extreme Adaptive Optics (SCExAO). Our observations and several differential-imaging reductions detected the ring and multiple spirals. We also newly detected darkening features on the ring and one of the spirals. Section 2 describes our observation, data reduction, and results. We then implemented radiative transfer modeling from *J* to *K* band and investigated scattering profiles. Our spiral fitting shows very large pitch angles ( $\sim 30^\circ$ – $50^\circ$ ), and we discuss possible scenarios that can induce multiple spirals with such large pitch angles. Details of each topic are investigated in Section 3. Finally we summarize our work in Section 4.

## 2. Data

### 2.1. Observations

We used Subaru/SCExAO+CHARIS in broadband IFS mode ( $1.16$ – $2.37 \mu\text{m}$ , spectral resolution of  $\mathcal{R} \sim 19$ , pixel scale =  $0''.0162 \text{ pixel}^{-1}$ ). In this paper we collapse the reduced IFS data cube into *JHK*-band images to discuss simultaneous multiband imaging results. HD 34700 A (*J* = 8.04, *H* = 7.71, *K* = 7.48; Cutri et al. 2003) was observed on 2019 January 12 UT with a Lyot coronagraph mask to suppress the starlight and a fixed pupil so that angular differential imaging (ADI; Marois et al. 2006) could be applied afterward. HR 2466 (*J* = 5.03, *H* = 5.07, *K* = 5.11; Cutri et al. 2003) was also observed for a point-spread function (PSF) reference of reference-star differential imaging (RDI; Lafrenière et al. 2009). Details about the data reduction are explained in Section 2.2. Astrogrids made from the star’s PSF were added in the field of view (FOV) with 25 nm amplitude modulation in the deformable mirror (Jovanovic et al. 2015; Sahoo et al. 2020), which provides accurate measurements of the central star’s location and photometry. The data were taken under very good seeing conditions ( $\theta_v \sim 0''.4$ ) and a typical FWHM was  $\sim 30$  (2 pix), 45, 55 mas in *JHK* bands, respectively. The total exposure time



**Figure 1.** Comparison of a single exposure for HD 34700 A (left) and HR 2466 (right) at channel 11 ( $\lambda = 1.6296 \mu\text{m}$ ). The color scale is arbitrary and these images are not rotated to north up. Astrogrids are located by the four edges in each FOV. The dashed black circle in each image indicates the coronagraph mask (113 mas in radius).

was 2168.6 s ( $1.475 \text{ s single exposure} \times 21 \text{ coadds} \times 70 \text{ cubes}$ ) for HD 34700 A and 2952.95 s ( $1.475 \text{ s single exposure} \times 14 \text{ coadds} \times 143 \text{ cubes}$ ) for HR 2466. The HD 34700 A observation obtained  $\sim 28^\circ$  of parallactic angle change for ADI.

### 2.2. Data Reduction and Results

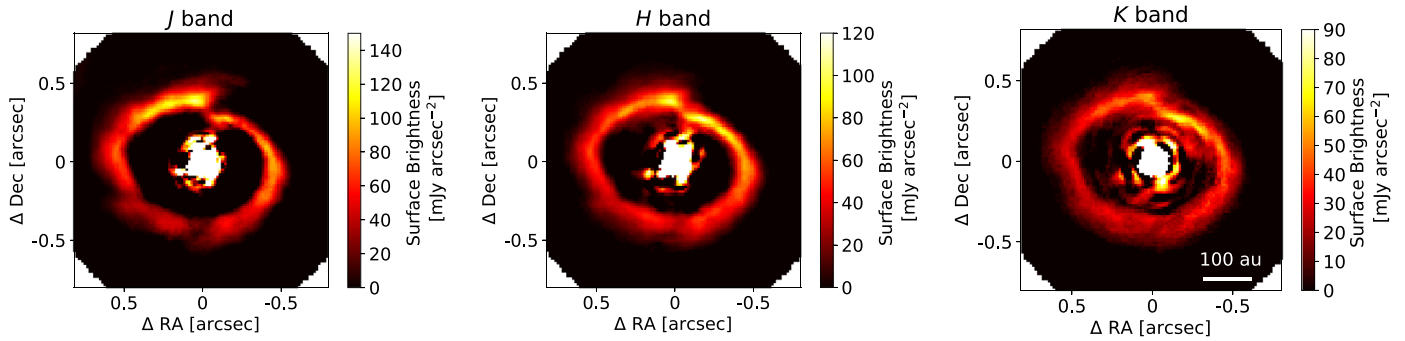
We used the CHARIS data reduction pipeline with the  $\chi^2$  extraction algorithm (Brandt et al. 2017) to extract dark-subtracted, flat-fielded, and wavelength-calibrated data cubes with 22 uniform spectral channels from the CHARIS raw files for both HD 34700 A and HR 2466. For spectrophotometric calibration we used appropriate Kurucz model atmospheres (Castelli & Kurucz 2003), adopting G0V and A2V for the spectral types of HD 34700 A and HR 2466 respectively. Single extracted data cubes show the ring feature of HD 34700 A without any postprocessing (Figure 1).

For postprocessing PSF subtraction we implemented two reduction techniques: (1) RDI by following the way of Currie et al. (2019) to capture the ring morphology without self-subtraction; (2) a combination of ADI and spectral differential imaging (SDI; Vigan et al. 2015) by following the way of Currie et al. (2018) to get high enough contrast to investigate outer spirals and potential planetary-mass companions. In both data reductions we used the same data reduction pipelines as Currie et al. (2018, 2019). Our methods are described in more detail below.

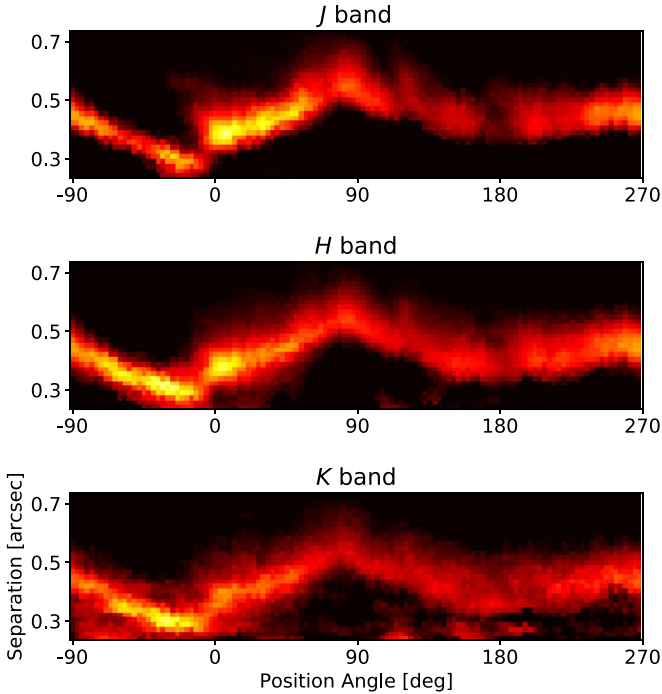
#### 2.2.1. RDI

First, we performed RDI by utilizing Karhunen–Loève image projection algorithms (KLIP; Soummer et al. 2012), where we adopted a “full-frame subtraction” on the CHARIS FOV ( $r_{\text{min}} = 3 \text{ pix}$  for the inner working angle,  $r_{\text{max}} = 65 \text{ pix}$  ( $1''.05$ ) for the outer working angle, and  $\Delta r = 62 \text{ pix}$  for the subtraction separation).

Figure 2 compares collapsed *JHK*-band ( $1.154$ – $2.387 \mu\text{m}$ ) images of RDI-reduced (Karhunen–Loève – the number of basis vectors;  $\text{KL} = 5$ ) HD 34700 A data and Figure 3 shows polar-projected images of Figure 2. Here we excluded channels (channels No. 6–8:  $1.3746$ – $1.4714 \mu\text{m}$ , No. 15–17:  $1.8672$ – $1.9987 \mu\text{m}$ ) that have stronger telluric absorption and lie either in the wings or outside of the nominal *JHK* bandpasses. We were able to resolve scattered light from the ring surface, but did not confirm an inner arc in the gap that Monnier et al. (2019) reported. Regions interior to  $\sim 240$ , 280, and 300 mas in *J*, *H*, and *K* bands are dominated by residual speckle noise in our RDI reduction. Thus, we focus on characterizing disk features at



**Figure 2.** RDI-KLIP ( $KL = 5$ ) reduction results in  $J$  (left),  $H$  (center), and  $K$  (right) bands. The central unresolved binary (HD 34700 Aab) is masked by the reduction algorithm. North is up and east is left.



**Figure 3.** Polar-projected (east of north) images of Figure 2 at the ring area. The color scale is set the same as in Figure 2.

wider separations (Section 3). Details about the ring feature are discussed in Section 3.

The ring extends along the whole azimuthal direction and shows some asymmetric features such as darkening, which makes it difficult to calculate a radial noise profile to define error bars of the surface brightness. Therefore, we calculate standard deviations at the interior ( $0''.3$ ) and exterior ( $0''.7$ ) of the ring in each collapsed image and we defined noise at the ring separation as interpolation of the standard deviations between the two separations. Here we adopted  $3\sigma$  clipping to mitigate effects of the presence of the ring at  $\sim 0''.3$  and the spirals at  $\sim 0''.7$ . The scattering properties of the ring are discussed in detail in Section 3.3.

### 2.2.2. ADI+SDI

After the basic reductions as mentioned at the beginning of Section 2.2, we performed ADI reduction utilizing the algorithms Locally Optimized Combination of Images (LOCI; Lafrenière et al. 2007) and Adaptive-LOCI (A-LOCI; Currie et al. 2012). A smaller separation of subtraction zones ( $\Delta r =$

$5$  pix) than the RDI reduction, a singular value decomposition (SVD) cutoff to truncate the diagonal terms of the covariance matrix of  $SVD_{\text{lim}} = 10^{-6}$  (see also Currie et al. 2013, 2018), a rotation gap of  $\delta = 0.75$  to limit signal loss/biasing due to azimuthally displaced copies of the astrophysical signal, and a pixel mask over the subtraction zone (e.g., Currie et al. 2012) were adopted to generate weighed reference PSFs at different separations. To further suppress residual speckles and achieve higher contrast we then performed SDI reduction on the ADI residuals.

Figures 4 and 5 show  $J$ ,  $H$ , and  $K$ -band images reduced using ADI+SDI instead of RDI (see Figures 2 and 3). We were able to detect several spiral features that are not detected by the RDI reduction (signal-to-noise ratios (S/Ns)  $\geq 4$  along the spines of the spirals)<sup>29</sup>. Details of the spiral fitting are described in Section 3.1.3.

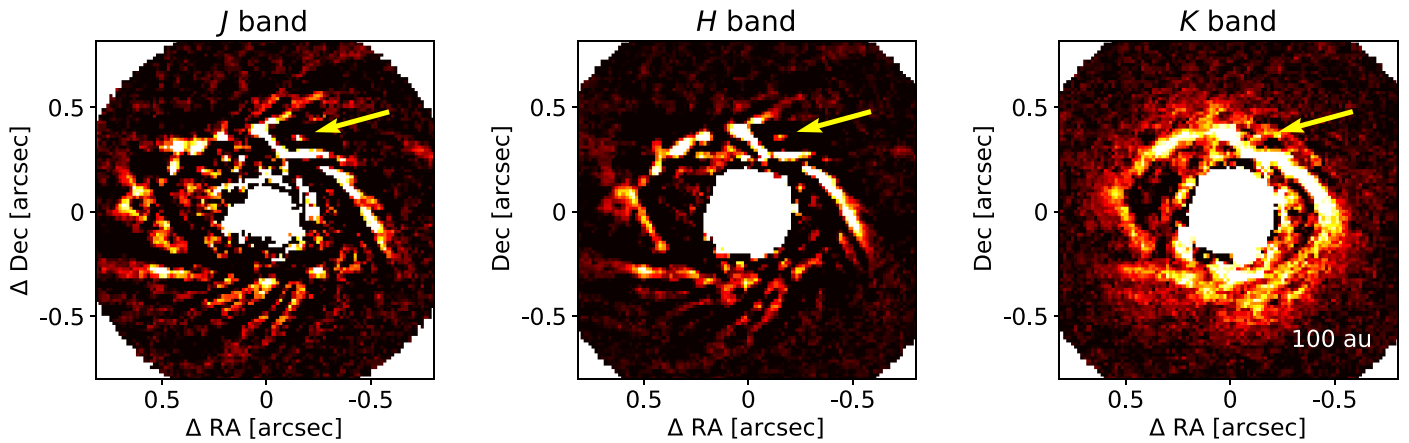
### 2.3. Constraints on Potential Companions

Our data did not reveal any substellar-mass companion candidates. We determined contrast limits by calculating radial noise profiles at each spectral channel, as in prior studies (Currie et al. 2011), including a correction for small sample statistics (Mawet et al. 2014). We took account of throughput correction by estimating flux loss of injected fake point sources made by the ADI+SDI reduction. We note that noise in this section is different from the noise of surface brightness used in Sections 2.2.1 and 2.2.2 because we aim at constraining point sources and thus used convolved images with aperture radii =  $FWHM/2$ . Figure 6 shows  $5\sigma$  contrast limits of our ADI+SDI reduction results and comparison with mass units at each band assuming a hot-start model (COND03; Baraffe et al. 2003) and 5 Myr. The broadband contrast achieved  $10^{-4}$  ( $\sim 12 M_{\text{Jup}}$ ) at  $0''.3$  and  $10^{-5}$  ( $\sim 5 M_{\text{Jup}}$ ) at  $0''.75$ . The detection limits are strongly affected by the bright ring and spirals at separations  $\gtrsim 0''.4$ , which bias an estimate of the noise.  $K$ -band contrast limits are poorer than  $JH$ -band limits because of the thermal background at channels of longer wavelength. With a cold-start model (Spiegel & Burrows 2012) a  $10 M_{\text{Jup}}$  object corresponds to  $\sim 10^{-7}$  contrast at each band and we do not compare our detection limits with the cold-start model.

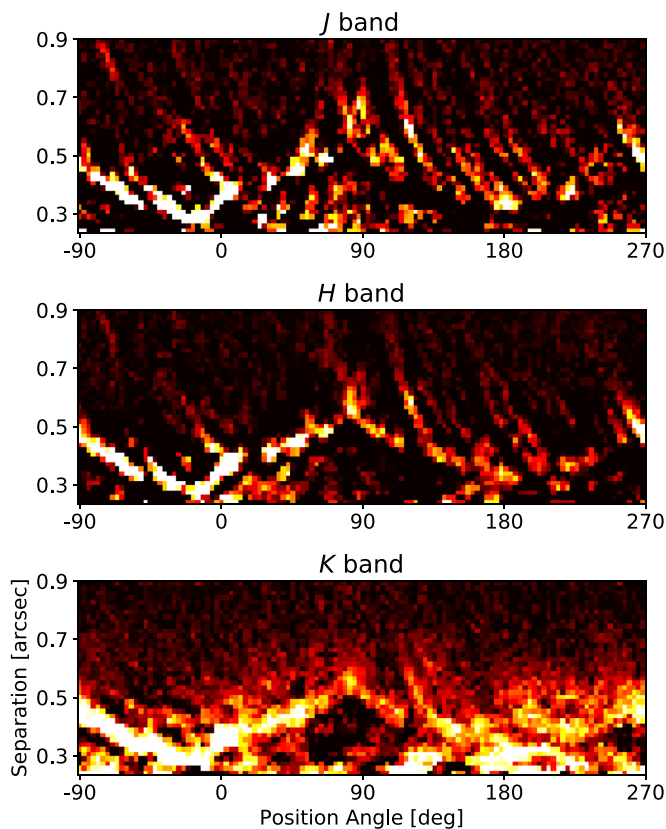
To test a hypothesis of an eccentric ( $e = 0.2$ )  $50 M_{\text{Jup}}$  companion embedded in the disk (Monnier et al. 2019), we injected a fake source in the CHARIS data set and reran the ADI+SDI reduction. For a spectrum we made a planet model

<sup>29</sup> The noise is defined as standard deviation at separations between  $0''.75 - FWHM/2$  and  $0''.75 + FWHM/2$  in each ADI+SDI-reduced image.



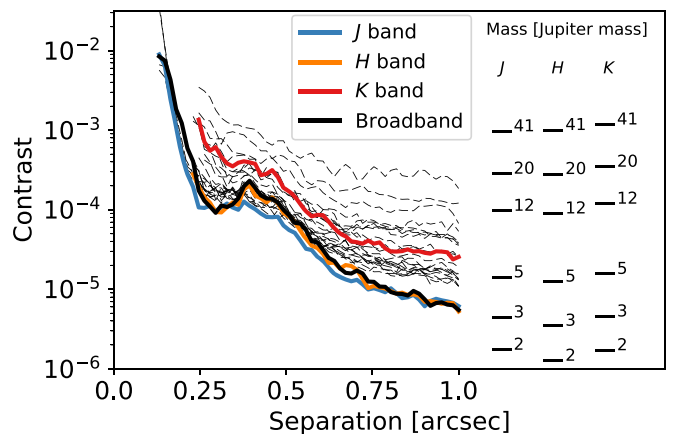


**Figure 4.** Same comparison of the reduced images as Figure 2 with ADI+SDI-A-LOCI reduction. The color scale is arbitrary. A positive signal at a similar location to where Monnier et al. (2019) predicted a substellar-mass companion, which is likely a part of the disk distorted or an artifact introduced by the ADI+SDI reduction, is indicated by a yellow arrow in each image (see Section 2.3 for details).



**Figure 5.** Same as Figure 3 for Figure 4 at the ring+spiral area.

among *JHK* bands by assuming *H*-band contrast of  $10^{-2.8}$ , which corresponds to  $0.05 M_{\odot}$  and  $\sim 2800$  K at 5 Myr in the COND03 model, using DH Tau B’s spectrum based on the VLT/SINFONI spectral library (Bonnetfoy et al. 2014). For a location we injected the fake source at  $0''.35$  north and  $0''.1$  west from the center (see also Figure 14 in Monnier et al. 2019). Figure 7 shows the ADI+SDI images with the injected fake source indicated by the dashed yellow circle. Compared with the actual ADI+SDI result the fake source can clearly be seen and self-subtraction by this source distorts the nearby ring shape. Therefore we conclude that our observation could set a robust constraint on the potential substellar-mass companion that Monnier et al. (2019) predicted. We note that there is



**Figure 6.**  $5\sigma$  contrast limits of our ADI+SDI result. Dashed lines correspond to that at each slice and *J*, *H*, *K*, and broadband (*JHK*) correspond to those of collapsed images at each wavelength, respectively. We also plot mass as a function of contrast at three wavelengths assuming COND03 and 5 Myr.

indeed a positive, albeit much fainter, signal at a similar location (indicated by yellow arrows in Figure 4). These signals are elongated and not significant among all the CHARIS channels. The RDI result did not detect any counterpart, so this is likely part of the disk feature distorted or an artifact introduced by the ADI+SDI reduction.

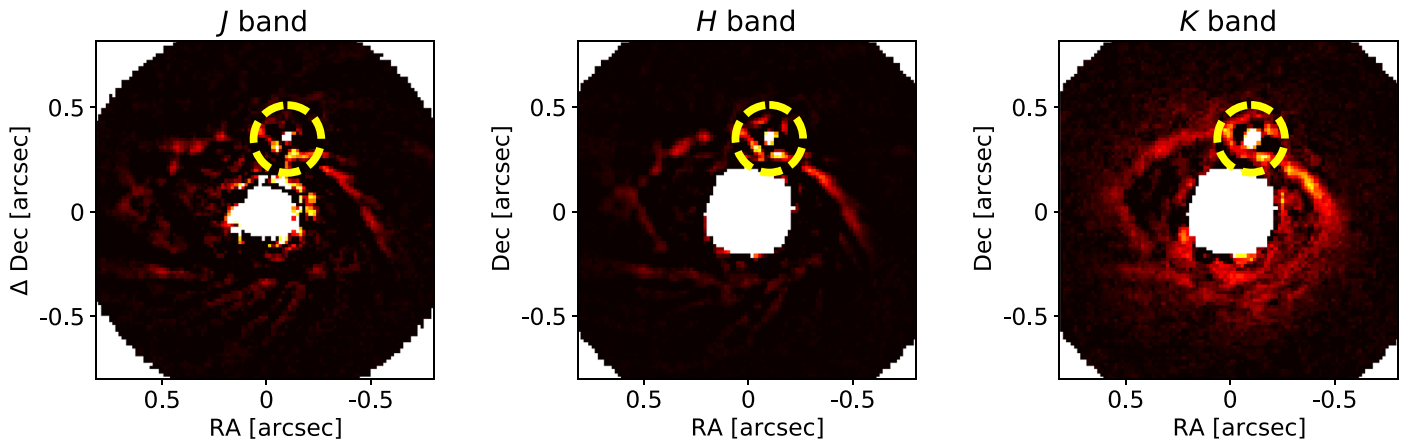
### 3. Analysis and Discussion

#### 3.1. Disk Morphology

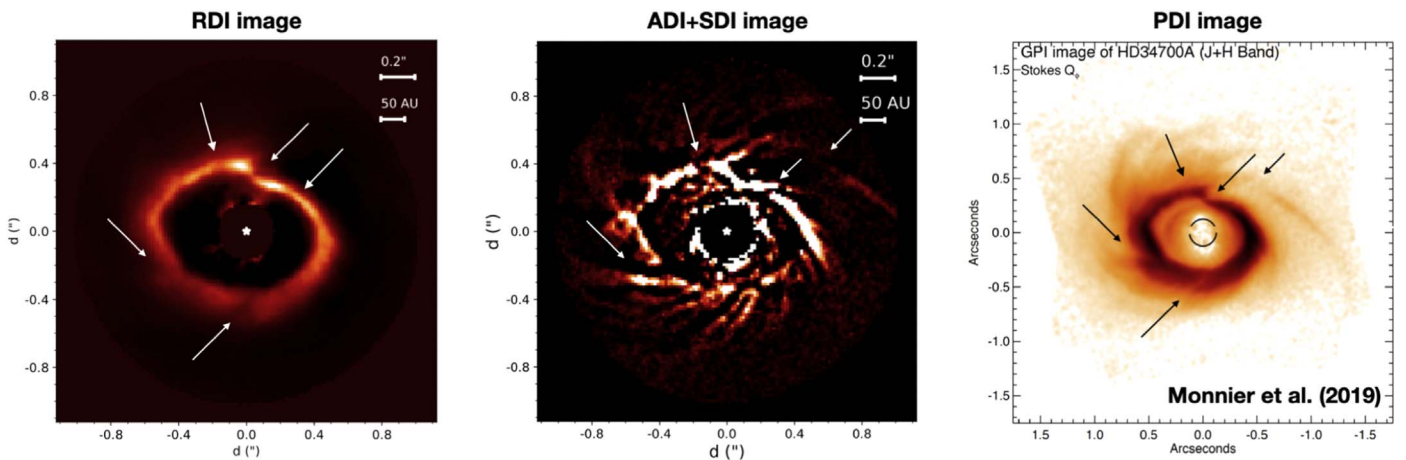
Figure 8 compares our new ADI+SDI and RDI images of HD 34700 A to the GPI-polarimetric differential imaging (PDI) result shown in Monnier et al. (2019). In this subsection we describe the ring, darkening features, and spirals in detail.

##### 3.1.1. Ring

We estimate that the RDI process alters the signal less than  $\sim 15\%$  (see Section 3.2), and thus we use the RDI images for our analysis. We fit the bright edge of the cavity to an ellipse using the Python ellipse fitting tool described in Hammel & Sullivan-Molina (2020). We provided as input to the Python routine the pixel coordinates of the local radial maxima in the surface brightness profiles in  $1^\circ$  wide azimuthal sections (cyan



**Figure 7.** As Figure 4 with an injected fake source (indicated by dashed yellow circles) to test the hypothesis of a  $50 M_{\text{Jup}}$  companion. We changed the color scale from Figure 4 to clearly show the injected source.



**Figure 8.** Comparison of the collapsed RDI and ADI+SDI images to the GPI-PDI image Monnier et al. (2019), reproduced by permission of J. Monnier. The arrows indicate darkening features (see Section 3.1.2). The central star is indicated by a white star in the masked region.

points in Figure 9(a)). We performed the fit separately on the  $J$ -,  $H$ -, and  $K$ -band RDI images (Figure 3) and found consistent results. The uncertainties on each parameter of the ellipse were obtained in each band using the standard deviation of the Gaussian fit to the distribution of fitting results for 10,000 bootstraps. Our final results are an average of the best fits obtained in each band, with the uncertainties for each band combined in quadrature. We found a semimajor axis of  $487.1 \text{ mas} \pm 2.7 \text{ mas}$  ( $173.6 \text{ au} \pm 1.0 \text{ au}$ ) and a shift of the center of the ellipse with respect to the star of  $52.7 \text{ mas} \pm 2.3 \text{ mas}$  toward a position angle (PA) of  $110^\circ.8 \pm 2^\circ.4$ .

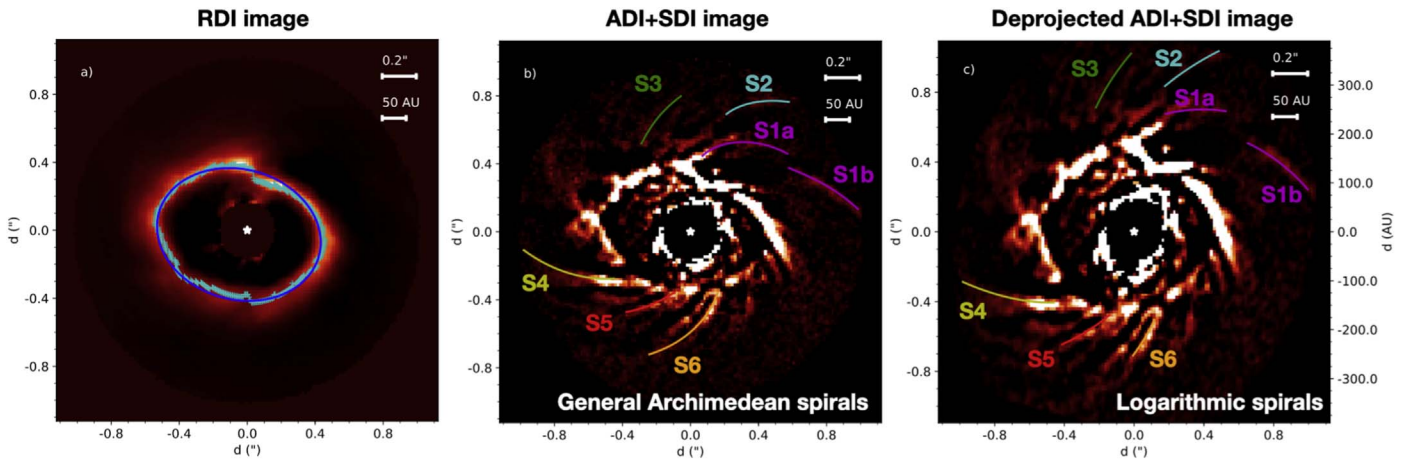
Assuming that the actual shape of the cavity is circular, our best-fit ellipse suggests a disk inclination of  $40^\circ.9 \pm 0^\circ.8$  and PA of semimajor axis of  $74^\circ.5 \pm 1^\circ.0$ . Regarding the uncertainty of PA we include the fitting uncertainty and CHARIS uncertainty on true north ( $0^\circ.27$ ; see Appendix A of Currie et al. 2018). Our estimates of the cavity parameters and the disk inclination are all consistent with those inferred in Monnier et al. (2019) using a similar method applied to the PDI image, apart from the value of the PA of the semimajor axis of the disk (for which they found  $69^\circ.0 \pm 2^\circ.3$ ). The slight discrepancy might be due to the difference in the scattering phase function between polarized intensity and total intensity. However, such a difference can stem from the requirement for the shift of the center of the ellipse with respect to the star to lie along the semiminor axis in their

procedure. Considering the uncertainties on the centering of the star and the assumption of a circular cavity, we did not force this condition in our procedure.

We note that the assumption of a circular cavity is not necessarily correct, given that several disks with large cavities show a nonnull eccentricity, such as HD 142527 and MWC 758 (Avenhaus et al. 2014; Dong et al. 2018b). New data from the Atacama Large Millimeter/submillimeter Array (ALMA) probing the kinematics of the disk would provide an independent estimate of its inclination. The difference in inclination, if any, estimated from the scattered light and ALMA will suggest a different distribution of gas/small grains/large grains and therefore we can determine whether the assumption of a circular cavity is reasonable.

### 3.1.2. Darkening Effects

The RDI images show evidence for multiple darkening areas on the bright edge of the cavity, and these areas, except for the northwest one, coincide with the GPI-PDI image and are indicated by arrows in Figure 8. We also indicate these regions by gray shades in plots of surface brightness and geometric albedo of the ring (see Figure 11 and Section 3.3 for details). We first note that the darkening features on the ring, except the northwest one, are located by the roots of S1, possibly S3, S4,



**Figure 9.** (a) Fit of the ring to an ellipse (blue curve) overlaid on the *JHK* band-collapsed RDI image. Cyan crosses show local radial maxima used for the fit. (b) Fit of the spiral arms seen in the collapsed ADI+SDI image to the equation of a general Archimedean spiral. (c) Deprojected ADI+SDI disk image (assuming a thin disk), where the spirals are fit to the equation of a logarithmic spiral, in order to estimate their pitch angle. In all images the central star is indicated by a white star.

and S6 (see also Figure 9). Shadows, actual geometric features, or other scattering characteristics due to heterogeneous dust distribution may explain the darkening features. We individually investigate the possibility of the shadowing effect for each darkening feature but do not rule out other possibilities. We also note that reproducing all the darkening features by only the shadowing effect likely requires multiple inner disks, which may be dynamically unstable. It is hard to identify which mechanism is the most favorable for reproducing each feature in this study.

Prominent, roughly symmetric shadowing effects can be seen to the north and south, at PA spanning  $\sim -25^\circ$  to  $30^\circ$  and  $\sim 155^\circ$  to  $200^\circ$ , and to the northwest and southeast, at PA spanning  $\sim 105^\circ$  to  $120^\circ$  and  $\sim 290^\circ$  to  $325^\circ$  ( $-70^\circ$  to  $-35^\circ$ ), respectively. There might be other possible darkening areas that are marginally seen in our reduced images and the surface brightness profile (e.g., PA  $\sim 210^\circ$  in the *J* band), but they are less convincing than those mentioned above and we do not conclude that such possible features are shadows or spiral roots in this study. The effect of the north–south symmetric shadows is seen in all bands, albeit more strongly at a shorter wavelength. The other pair is only seen in the *J* and *H* bands, suggesting that it is optically thin at longer wavelength (Figure 3 and 11) or has different scattering characteristics (in this case the darkening feature corresponds to a non-shadowing effect). These darkening features can also be seen in our ADI+SDI image, although less conspicuously given the presence of radial postprocessing artifacts (left panel of Figure 8). Furthermore, our ADI+SDI image suggests shadowing of a part of the main northwest spiral, which appears to lie in the continuity of the northern part of the symmetric north–south shadow.

A comparison of our images to the PDI image shown in Monnier et al. (2019) confirms the presence of all darkening areas, except one in the northwest direction, in their image too (right panel of Figure 8)—albeit not reported as such. The symmetric shadows are reminiscent of polarimetric imaging or space-based coronagraphic imaging of the disks such as HD 142527 (Avenhaus et al. 2014; Marino et al. 2015), HD 100453 (Benisty et al. 2017), HD 163296 (Wisniewski et al. 2008; Rich et al. 2019), SAO 206462 (Stolker et al. 2017), and DoAr 44 (Casassus et al. 2018), and suggest the presence of an inclined inner disk. These shadow features may

also be reproduced by a combination of single shadows. The single shadow is reminiscent of the ones observed in the circumbinary disk of GG Tau A, which includes a close central binary similar to HD 34700 A (Itoh et al. 2002, 2014), and in the transition disk of HD 169142 (Quanz et al. 2013; Bertrang et al. 2018). Several explanations for the single shadow of GG Tau have been proposed, including a dense clump in an accretion stream onto one component of the central binary, or a circumplanetary disk surrounding a protoplanet located in the cavity (Krist et al. 2002; Canovas et al. 2017) as well as circumstellar disks around GG Tau Aa/b (Brauer et al. 2019; Keppler et al. 2020).

Finally we note that our observation did not detect any further inner object(s) down to  $\sim 0''.2$ . ALMA continuum observation may help to investigate possible inner disk(s). Follow-up high-contrast observations are also useful to investigate time variation of the shadows and to constrain inner objects because previous observations reported (possible) changes of shadow features (on a timescale of years; Wisniewski et al. 2008; Debes et al. 2017; Stolker et al. 2017; Uyama et al. 2018; Rich et al. 2019; Laws et al. 2020). Assuming that an inner object at a radius of  $0''.2$  (73 au, slightly interior to the physical inner working angle in our *J*-band result) casts a shadow on the ring ( $0''.5$ ) and that we can identify the time variation of the shadow if the shadow shifts by 30 mas (= *J*-band angular resolution in our observation), the inner object should move 12 mas (4.4 au). A period of Keplerian rotation at 73 au around HD 34700 A is about 313 years and the 4.4 au movement takes 3 yr. A discussion of color in the darkening areas with the high-contrast imaging may also help to investigate whether possible inner object(s) are optically thick or thin. If the darkening areas are accompanied by actual geometric features the scattered light there might include multiple scattering, a proportion of which depends on dust properties (e.g., Takami et al. 2013), and then detailed discussions with radiative transfer simulations are required for a synthetic understanding of HD 34700 A’s disk.

### 3.1.3. Spiral Characterization

To increase the S/Ns of the faint spirals we used a median-combined ADI+SDI image using all CHARIS spectral channels. Although the ADI+SDI reduction can cause self-



**Table 1**  
Pitch Angle of the Spirals

Spiral	$\phi$ (deg)	$\phi_{\text{deproj, thin}}$ (deg)	$\phi_{\text{deproj, } h=0.3r}$ (deg)
S1a	$31.3 \pm 1.0$	$34.7 \pm 1.4$	$46.9 \pm 1.2$
S1b	$40.2 \pm 1.4$	$27.0 \pm 1.9$	$27.1 \pm 1.5$
S2	$37.1 \pm 2.6$	$51.9 \pm 2.0$	$62.8 \pm 0.9$
S3	$34.4 \pm 2.8$	$48.5 \pm 3.3$	$61.0 \pm 0.8$
S4	$53.9 \pm 1.7$	$49.4 \pm 1.8$	$51.4 \pm 1.7$
S5	$50.2 \pm 1.2$	$54.7 \pm 3.8$	$51.0 \pm 1.4$
S6	$41.3 \pm 0.9$	$53.2 \pm 2.0$	$44.9 \pm 0.9$

subtraction of the spiral features, our data reduction adopts reasonable settings to avoid biasing the actual morphology (see Section 2.2.2 for the settings). The rotation gap ( $\delta = 0.75$ ) limits the self-subtraction of the astrophysical signal caused by rotating the field. With a local pixel-masking over the subtraction zone, the astrophysical signal contained within the subtraction zone does not bias the LOCI coefficients and self-subtraction is reduced (for details see Currie et al. 2018).

We followed the same procedure as in Reggiani et al. (2018) and Price et al. (2018) to identify the trace of spiral arms as local maxima in the radial intensity profile of the disk, and fit them using the equations of general Archimedean and logarithmic spiral arms, respectively. The fits to the equation of general Archimedean spirals systematically yield the best morphological match, while the fit to logarithmic spirals is used to estimate pitch angle. In polar coordinates, a general Archimedean spiral is given by the equation  $r = a + b\theta^n$ , and a logarithmic spiral by  $r = r_0 e^{k\theta}$ , where the pitch angle ( $\phi = \arctan(k)$ ) is constant and determines the spiral. With this procedure, we fit the six brightest spirals outside the ring, including two arcs likely tracing the same spiral but truncated due to shadowing from the inner disk (referred to as S1a and S1b). All the identified spirals have  $S/N \gtrsim 4$  at their spines, except S3 ( $S/N \sim 3\text{--}3.5$ ), in the collapsed ADI+SDI image. The first column in Table 1 reports the pitch angle measured for each spiral arm labeled in Figure 9.

Given that the disk is inclined, if the spirals are located in the same plane as the inner edge of the outer disk (i.e., the bright ring), one has to measure spiral pitch angles in the deprojected image of the disk for a meaningful comparison to the values predicted by different spiral formation mechanisms. We deprojected the image with respect to the center of the disk, i.e. considering the 52.7 mas shift with respect to the location of the star, and considering the values of inclination and PA of semimajor axis inferred in Section 3.1.1:  $40^\circ.9$  and  $74^\circ.5$ , respectively. The pitch angles measured in the deprojected image are provided in the middle column of Table 1. Deprojection in this way ignores the vertical characteristics of the spiral feature. For comparison we made another deprojected image with diskmap (Stolker et al. 2016) by taking into account a large constant opening angle ( $h(r) = 0.3r$ , where  $h$  is the height of the scattering surface) and then conducted the spiral fitting, the results of which are also given in the last column of Table 1. The difference is significant along the semiminor axis (S1a, S2, S3, and S6). We note that our spiral fitting may also be affected by the inclination of HD 34700 A’s disk. Dong et al. (2016) suggested that scattered light of the spiral feature can be distorted by its inclination, and image deprojection by  $\sim 40^\circ$  may not trace the real spiral feature.

**Table 2**  
Disk Model Parameters

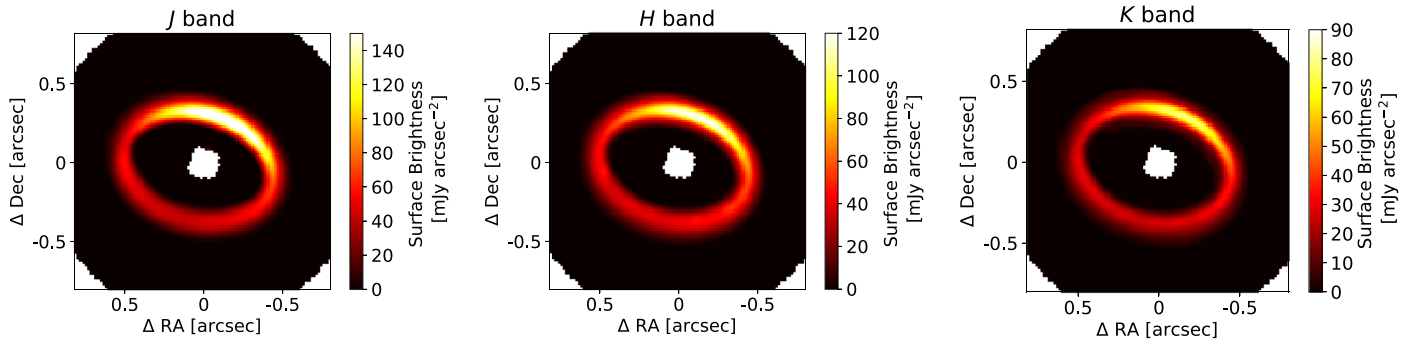
Disk Parameter	Value
Distance* (pc)	365.5
$T_{\text{eff}}^*$ (for Aa, Ab) (K)	5900, 5800
$L_*^*$ (for Aa, Ab) ( $L_\odot$ )	13, 11.5
$R_*^*$ (for Aa, Ab) ( $R_\odot$ )	3.46, 3.4
$M_*^*$ (for Aa, Ab) ( $M_\odot$ )	2.0, 2.0
Separation between Aab* (au)	0.69
$A_V^*$	0.0
Disk position angle ( $\theta$ ) (deg)	60
Disk inclination ( $i$ ) (deg)	40.9
Disk offset from star—major axis (au)	−10
Disk offset from star—minor axis (au)	5
Inner radius, $R_{\text{in}}$ (au)	170
Outer radius, $R_{\text{out}}$ (au)	400
Disk wall radius, $R_w$ (au)	200
Scale height at inner radius, $H_{\text{0, in}}$	0.1
Scale height power law, $p_{\text{gas}}$	1.2
Radial surface density power law ( $\epsilon$ )	0.5
Wall shape ( $w$ )	rounded/0.2
$M_{\text{dust}}$ ( $M_\odot$ )	$2.5 \times 10^{-4}$
Minimum dust size ( $a_{\text{min}}$ , $\mu\text{m}$ [small, large])	0.25, 5
Maximum dust size ( $a_{\text{max}}$ , $\mu\text{m}$ [small, large])	5, 1000
Dust size power law, $p_a$	3.5
Dust carbon mass fraction	0.1
Dust silicate mass fraction	0.9

**Note.** We fixed stellar parameters (with \* symbol) to those estimated in Monnier et al. (2019). The dust mass is evenly divided between “small grain” and “large grain” components. The wall shape parameter defines the spatial scale over which the disk surface density increases from  $R_{\text{in}}$  to  $R_w$ . See Mulders et al. (2010, 2013) and Thalmann et al. (2014) for detailed explanations of the MCM3D terminology.

The values of pitch angle in Table 1 are significantly discrepant with the rough estimates of  $20^\circ\text{--}30^\circ$  reported in Monnier et al. (2019). Since they do not mention how the pitch angles were measured nor whether a deprojection was performed for their measurement, it is difficult to discuss the reason for this discrepancy. From the deprojected pitch angles of Table 1 in a thin-disk case, we notice a significant difference between S1 ( $\phi_{\text{deproj}} \sim 30^\circ$ ) and the other spirals ( $\phi_{\text{deproj}} \sim 50^\circ$ ), possibly pointing to different origins. In a thick-disk case the pitch angle of S1b is significantly different to that of other spirals. S1b is located at a larger separation from the ring and it might have different characteristics than the other spirals. We note that ADI+SDI reduction could cause distortion of the real shapes because of self-subtraction, and follow-up observations with ALMA or high-contrast PDI/RDI reductions with a comparable angular resolution and sensitivity will help to confirm our result of the spiral fitting.

### 3.2. Forward Modeling

To investigate the disk’s scattering profile, we use forward modeling to reproduce the observed ring with a synthetic scattered light disk and simultaneously match most of the system’s spectral energy distribution. Here we do not include probable shadowing effects due to inner disk(s). We followed Currie et al. (2019) with the MCM3D radiative transfer code (Min et al. 2009) to model the ring and compared the forward-modeled disk with the CHARIS-RDI result. We adopted the best-fit parameters in Monnier et al. (2019) as initial parameters



**Figure 10.** The best-fit forward-modeled disks in the *J* (left), *H* (center), and *K* (right) bands. The images are convolved by the instrumental PSF and then reduced by the RDI reduction.

and then explored a small range of the model component parameters to reproduce the scattered light image.

Table 2 summarizes the best-fit model of the ring and Figure 10 compares the forward-modeled disks in the *JHK* bands. The surface density of the disk component follows

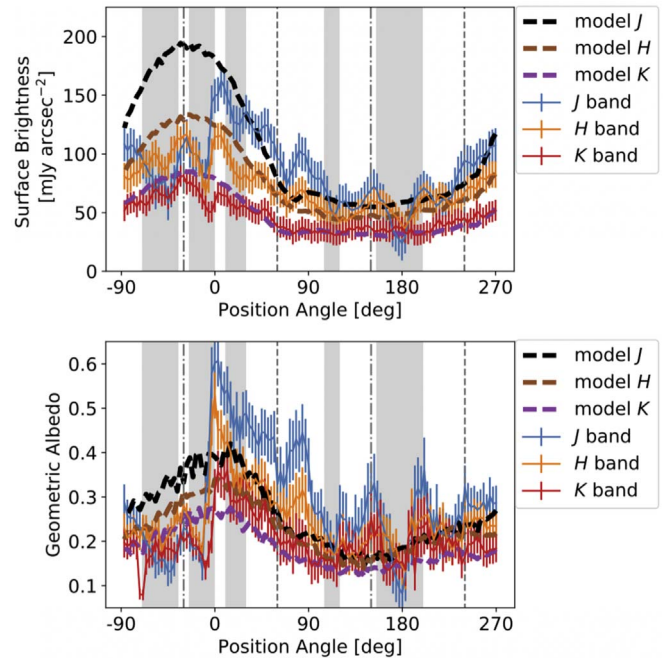
$$\Sigma(R < R_w) \propto R^{-\epsilon} \times \exp\left(-\left(\frac{1 - R/R_{\text{exp}}}{w}\right)^3\right) \text{ and } \Sigma(R \geq R_w) \propto R^{-\epsilon}.$$

The scale height in our model is consistent with the best-fit scale height without very small grains or polycyclic aromatic hydrocarbons in Monnier et al. (2019). Other best-fit parameters do not have large differences from those of Monnier et al. (2019) but our best-fit model provides a better match to the surface brightness (see Section 3.3 for details). We estimated attenuation factors by comparing the modeled disks before and after the KLIP-RDI reduction; these are used for throughput correction of the RDI reduction ( $\sim 10\%$ – $15\%$  flux loss at the ring peak). The throughput-corrected surface brightness of the ring is shown in Figure 11.

### 3.3. Scattering Profiles

Figure 11 compares azimuthal profiles of surface brightness and geometric albedo (see Equation (3) of Mulders et al. 2013) by tracing the peaks of the ring. Note that this geometric albedo depends on dust albedo and the geometry of the disk. Solid lines with errors correspond to the traced ring peaks from the collapsed *JHK*-band images after the throughput correction. Error bars are extrapolated from the background noise at  $0''.7$  (see Section 2.2.1). The dashed lines correspond to the ring peaks from the modeled disk before the RDI reduction.

The model matches the general trend in surface brightness very well except for the *J* band at  $\sim -90^\circ$  to  $0^\circ$ , large parts of which are affected by the darkening effects (see also Section 3.1.2), and better reproduces the total intensity of the resolved ring without weighting different passbands. Monnier et al. (2019) needed to multiply the *H*-band model by 2 to match the GPI result. We note that the model adopts a simple ellipse to approximately reproduce the ring geometry but the actual ring has more complex features such as the darkening features, the discontinuity at  $\text{PA} \sim 0^\circ$ , and the spirals. Compared with the GPI total intensity (Monnier et al. 2019) our azimuthal profiles are different in both *J* and *H* bands. This difference is mainly due to the difference in data reduction: Monnier et al. (2019) made an approximate reference PSF by assuming a Moffat function and subtracted it from the total intensity (star+disk) image to extract the disk total intensity, while we used the practical star (HR 2466) for a reference PSF

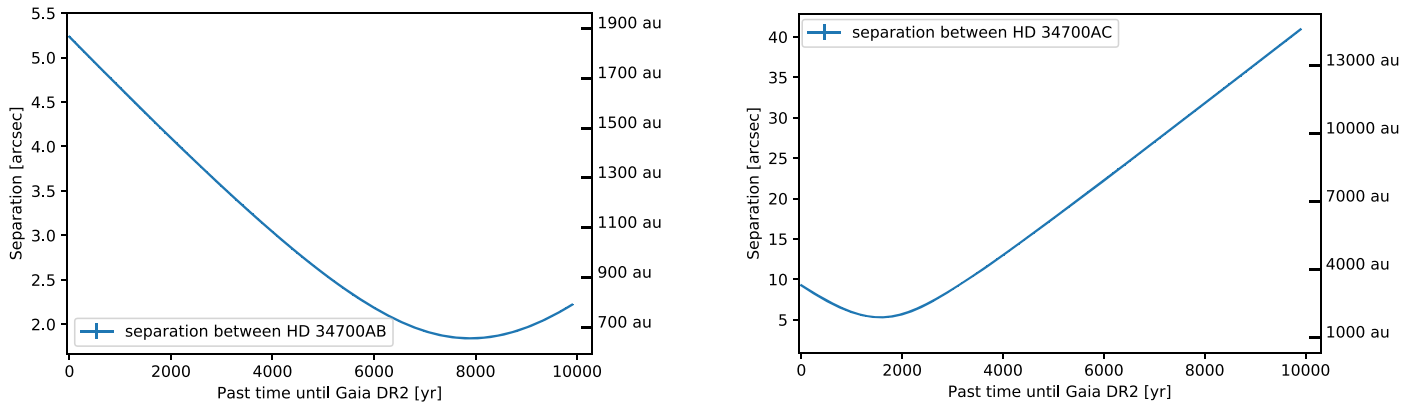


**Figure 11.** Azimuthal profiles of surface brightness after the throughput correction by tracing the ring peak (top) and geometric albedo converted from the surface brightness (bottom). Those profiles of the modeled disks are overlaid. Gray shaded areas indicate the darkening areas (see Section 3.1.2). Gray vertical dashed and dashed–dotted lines indicate the major and minor axes of the best-fit disk model respectively. Error bars in the top image correspond to 14.5, 11.3, and 8.93 mJy arcsec $^{-2}$  in the *J*, *H*, and *K* bands, respectively. Note that the model adopted a simple ring without the darkening effects, discontinuity, and spirals seen in the actual disk.

and conducted the RDI reduction. As HD 34700 A is a binary the source of light onto the disk surface is variable, which can also vary the scattering profile.

We used photometric results from the Two Micron All Sky Survey (Cutri et al. 2003) and deprojected separations (assuming the disk inclination of  $40^\circ.9$ —see Table 2) of the traced ring to convert surface brightness into the geometric albedo. The difference in the geometric albedo profiles between the resolved disk and the modeled disk looks larger than in the case of the surface brightness profile because the conversion includes the geometric difference between both the two disks (see Appendix A). A remarkable feature in the albedo plot is a color tendency at  $\text{PA}$  between  $\sim 45^\circ$  and  $90^\circ$ . The model-based geometric albedo is comparable in the *JH* bands, while the actual *J*-band geometric albedo has a higher value than that in the *H* band. Such a Rayleigh-scattering-like feature appears at





**Figure 12.** Projected separation between HD 34700 AB (left) and AC (right). Error bars include only measurement errors of R.A. and decl. (see also Figure B1).

greater scale height or where submicron dust is prominent, and our result suggests either or both of these possibilities in this area.

### 3.4. Origin of the Spirals

Spiral S1, particularly S1b, appears to be more tightly wound than the other spirals observed in the disk, with measured pitch angles of  $\sim 35^\circ$ – $47^\circ$  and  $\sim 27^\circ$  for the inner (S1a) and outer (S1b) sections (see Section 3.1.3), respectively. In a thin-disk case S1ab can have the same origin, and it is also interesting that S1 is the only spiral that is directly crossed by a shadow. Shadowing has been suggested as a possible mechanism to form spiral arms, due to the periodic temperature and hence pressure kick imprinted on material rotating in the disk (Montesinos et al. 2016; Montesinos & Cuello 2018). The morphology of S1a and S1b is roughly compatible with the inner and outer wakes of a spiral launched from a shadow, with a larger (resp. smaller) pitch angle for the inner (resp. outer) wake. In a thick-disk case S1ab might be disconnected and formed via different mechanisms. Future observation may help to investigate whether these spirals are physically connected or not.

The radially extended feature of S1 is also compatible with being launched by a companion. In that case, it is unlikely to be caused by a yet undetected companion in the cavity, as outer wakes are expected to be tightly wound ( $\phi \leq 10^\circ$ ; Bae & Zhu 2018). The large pitch angle of both S1a and S1b would suggest that they correspond to an inner spiral wake (with respect to the companion). This could be either a yet undetected protoplanet in the outer disk (e.g., Dong et al. 2015; Zhu et al. 2015) or the known K-dwarf outer companion HD 34700 B.

From their flocculent appearance, spirals S2–S6 ( $\phi \sim 50^\circ$ ) may resemble those seen in numerical simulations of gravitationally unstable protoplanetary disks (e.g., Rice et al. 2003). However, Monnier et al. (2019) estimated the Toomre parameter to be larger than 25 everywhere in the disk based on their radiative transfer model, which makes this possibility unlikely.

#### 3.4.1. Stellar Flyby

Considering the respective proper motion of HD 34700 AB, an interesting possibility is that of a recent flyby. Hydrodynamical simulations show that stellar flybys can induce spirals with a large pitch angle (e.g., Cuello et al. 2019, 2020). In practice arms/spirals in the RW Aur A and UX Tau A disks

can be well reproduced by the stellar flyby (Dai et al. 2015; Rodriguez et al. 2018; Ménard et al. 2020). We checked R.A., decl., and proper motions for HD 34700 A and B (Gaia Collaboration et al. 2018) and calculated their projected separation in the past. The separation ( $r$ ) between HD 34700 AB is expressed as follows:

$$r = \sqrt{(\Delta R.A._0 - \Delta pm_{R.A.} \times t)^2 + (\Delta Decl._0 - \Delta pm_{Decl.} \times t)^2},$$

where  $\Delta R.A._0$  and  $\Delta decl._0$  are differences in R.A. and decl. in Gaia DR2,  $\Delta pm_{R.A.}$  and  $\Delta pm_{decl.}$  are those in proper motions along R.A. and decl., and  $t$  corresponds to time [year]. We also checked the projected separation from HD 34700 C, which is located at  $\sim 9''.2$  from HD 34700 A. Current astrometric databases such as Gaia do not have a record of the proper motion of C and we approximately defined the proper motion as the difference between the values in Gaia DR2 and Sterzik et al. (2005), which may include systematic uncertainty of astrometry. The estimation of C’s proper motion requires the coordinate of A on 2004 January 30, when the observation of the HD 34700 system was made by Sterzik et al. (2005). We used `astropy.coordinates` libraries to extrapolate the position on this date from Gaia DR2 coordinates and proper motion. Monnier et al. (2019) suggested another companion candidate HD 34700 D, but a proper motion test with Hubble Space Telescope (HST)/STIS coronagraphic data taken in 2018 (PI: Marie Ygouf) revealed that this object is not comoving (M. Ygouf et al. 2020, in preparation). Therefore we do not investigate the stellar flyby scenario with D. We note that these estimations of the separations do not take orbital motions and star–companion interactions into account. Future studies with more inputs of the positions will help us to infer their orbits and to discuss the stellar flyby scenario in detail.

Figure 12 illustrates projected separations between HD 34700 AB (left) and AC (right). The left separation curve suggests a possibility that HD 34700 B could be located  $\sim 700$  au away from HD 34700 A. For the case of C the separation is greater than 1000 au and C may be less responsible for inducing the spirals than B. The larger relative proper motion of C than that of B may be affected by the systematic uncertainty between Gaia DR2 and Sterzik et al. (2005). We assume the same distance and do not take into account line-of-sight motion in these plots because Gaia-based distances are  $356.5_{-6.0}^{+6.3}$  pc and  $353_{-12}^{+10}$  pc for A and B respectively and are consistent with each other within errors. The parallax of C has

not been measured, and we adopted the same assumption about the distance. We note that errors of the separation increase as time increases (see Appendix B) if we include Gaia measurement errors of the proper motion, and that the error bars in Figure 12 include only measurement errors of R.A. and decl. Cuello et al. (2019) showed that spirals induced by a stellar flyby can survive for more than 7000 yr under some conditions, and stellar flyby is perhaps a reasonable scenario if HD 34700 B passed by HD 34700 A  $\sim$ 8000 yr ago. As we have large uncertainties in periastron and we do not set any constraints on the angle between the disk plane and the perturber plane (HD 34700 B’s orbit) we do not further simulate the disk feature with the stellar flyby scenario in this study.

### 3.4.2. Infall

An alternative possibility for the origin of the flocculent spiral pattern is infall from a late envelope or a captured cloudlet (e.g., Tang et al. 2012; Dullemond et al. 2019). A late-envelope infall was proposed to account for the similar spiral pattern observed in the disk of AB Aur (Fukagawa et al. 2004; Tang et al. 2012, 2017). Large-scale images of the environment of AB Aur show the presence of a large surrounding cloudlet, which led Dullemond et al. (2019) to propose that transitional disks such as AB Aur could all be the result of cloudlet capture. In that case, the spirals might be seen in a different plane than that of the inner rim of the outer disk, i.e., the outer disk would be warped, like HD 100546 for example (e.g., Quillen 2006). This would explain the very large deprojected values of pitch angle. We note that previous studies and our observation have not yet detected any envelope-like features. Monnier et al. (2019) implemented spectral energy distribution fitting of HD 34700 A and indicated  $A_v = 0$ . They also presented the large FOV image of HST/NICMOS ( $\sim 18''.9 \times 18''.9$ ) where one half of its vicinity was explored and there is no significant signal of an envelope. The HST/STIS data cover the whole vicinity (within a radius of  $\sim 10''$ ) and confirmed a faint halo extending outside the CHARIS FOV ( $\sim 2''$ – $3''$  in radius; Ygouf et al. 2019, and M. Ygouf et al. 2020, in preparation). We attempted to fit the traced peaks of the spirals with infall but could not set robust constraints on spiral parameters with the infall scenario because of large uncertainties (see Appendix C). CO rotational line observations with ALMA may help to investigate the kinematics of the outer disk, including the spirals.

Apart from AB Aur, HD 34700 A also shows a similar spiral pattern to the circumbinary disk HD 142527 (e.g., Fukagawa et al. 2006; Christiaens et al. 2014; Avenhaus et al. 2014). Both systems harbor a prominent spiral combined with multiple smaller flocculent spiral arms stemming from the edge of the cavity. The hydrodynamical simulations in Price et al. (2018) suggest that the dynamical interaction between the inner binary and the outer disk can account for the flocculent spiral arms in HD 142527. The prominent spiral might correspond to a secular large-scale spiral density wave (e.g., Demidova & Shevchenko 2015). However, the separation between the inner binary of HD 34700 Aa and Ab is significantly smaller than that of HD 142527 AB (0.69 au versus 25–50 au) for a similar size cavity ( $\sim 175$  au versus  $\sim 130$  au), so it is unclear whether the inner binary could reproduce all of the spirals of HD 34700 A. Dedicated hydrodynamical simulations are required to pinpoint the origin(s) of the spirals of HD 34700 A.

## 4. Summary

We have presented Subaru/SCEXAO+CHARIS broadband (*JHK* bands) IFS of the HD 34700 A protoplanetary disk. The observation was conducted under such good seeing conditions that a single frame could resolve the ring without any postprocessing. We then conducted RDI and ADI+SDI reductions to obtain its morphology and to estimate the surface brightness accurately, which resulted in clear detection of both the ring and multiple spirals as shown in Monnier et al. (2019). Although Monnier et al. (2019) suggested a  $50 M_{\text{Jup}}$  companion embedded in the disk, we did not detect any companion candidates. We calculated contrast limits from the ADI+SDI result, and the broadband contrast curve sets a constraint on potential substellar-mass objects down to  $\sim 12 M_{\text{Jup}}$  at  $0''.3$  (in the gap) and  $\sim 5 M_{\text{Jup}}$  at  $0''.75$  (outside the ring) assuming the COND03 model and 5 Myr. We also tested the  $50 M_{\text{Jup}}$  companion scenario by injecting a fake source and concluded that our observation could set a robust constraint on this hypothesis.

We used the MCM3D radiative transfer code to reproduce the ring scattering profile. By checking the reduced images and comparing surface brightness with the forward-modeled disk we newly confirmed darkening effects on the ring and spiral, large parts of which appear to be shadows cast by possible inner object(s). Except at these darkening features, our best-fit model provides a better match to the actual surface brightness among *JHK* bands than that of Monnier et al. (2019), which showed some discrepancy in the surface brightness. However, some of these features are located by the roots of the spirals, and we do not rule out other possibilities such as physical features related to the outer spirals. Geometric albedo converted from the surface brightness of the ring suggests a greater scale height and/or prominently abundant submicron dust at position angles between  $\sim 45^\circ$  and  $90^\circ$ .

We also conducted spiral fitting of S1–S6 and the result suggests very large pitch angles ( $\sim 30^\circ$ – $50^\circ$ ) that are larger than the estimated pitch angles presented in Monnier et al. (2019). A stellar flyby of HD 34700 B or infall from a surrounding envelope is perhaps a reasonable scenario to explain the large pitch angles. We investigated the separation between HD 34700 AB based on Gaia-based coordinates and proper motions, and HD 34700 B could be located  $\sim 700$  au away from HD 34700 A about 8000 yr ago. Future CO observations with ALMA may investigate the kinematics of the outer disk, including the spirals.

The authors would like to thank the anonymous referees for their constructive comments and suggestions to improve the quality of the paper. We thank John Monnier for authorization to use GPI-PDI images originally presented in Monnier et al. (2019). The authors are grateful to Gijs Mulders for helpful comments. This research is based on data collected at the Subaru Telescope, which is operated by the National Astronomical Observatories of Japan. This research has made use of NASA’s Astrophysics Data System Bibliographic Services. This research has made use of the SIMBAD database, operated at CDS, Strasbourg, France. This research made use of Astropy, a community-developed core Python package for Astronomy (Astropy Collaboration et al. 2013, 2018).

T.U. acknowledges JSPS overseas research fellowship. T.C. is funded by a NASA Senior Postdoctoral Fellowship. J.W. acknowledges funding support from the NASA XRP program

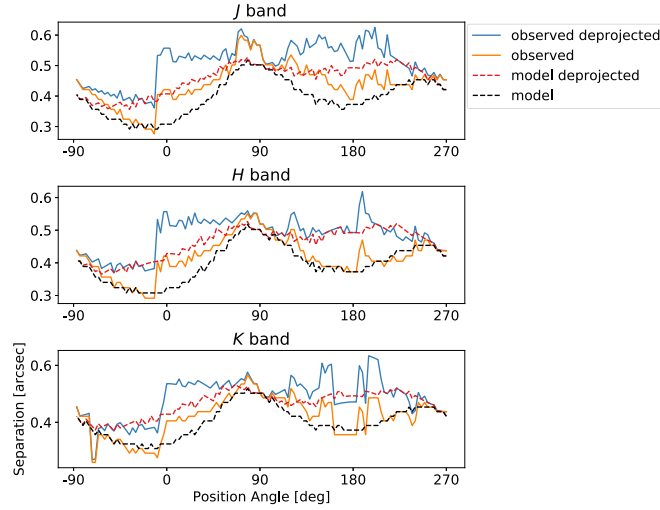
via grants 80NSSC20K0252 and NNX17AF88G. S.T. is supported by JSPS KAKENHI Grant-in-Aid for Early-Career Scientists No. 19K14764. M.T. is supported by MEXT/JSPS KAKENHI grant Nos. 18H05442, 15H02063, and 22000005. E.A. is supported by MEXT/JSPS KAKENHI grant No. 17K05399. The development of SCEXAO was supported by JSPS (Grant-in-Aid for Research #23340051, #26220704 & #23103002), Astrobiology Center of NINS, Japan, the Mt Cuba Foundation, and the director’s contingency fund at Subaru Telescope. CHARIS was developed under the support by the Grant-in-Aid for Scientific Research on Innovative Areas #2302.

The authors wish to acknowledge the very significant cultural role and reverence that the summit of Maunakea has always had within the indigenous Hawaiian community. We are most fortunate to have the opportunity to conduct observations from this mountain.

### Appendix A

#### Difference between Separations of the Traced Rings

Figure A1 shows peak loci of the resolved ring and the modeled ring in each band. The difference in disk geometry affects the conversion from surface brightness into geometric albedo in Section 3.3.



**Figure A1.** Comparison of peak loci between the resolved ring (“observed”—solid line) and the modeled ring (“model”—dashed line), overlaid with both deprojected separations (“deprojected”), in the *J*, *H*, and *K* bands.

### Appendix B

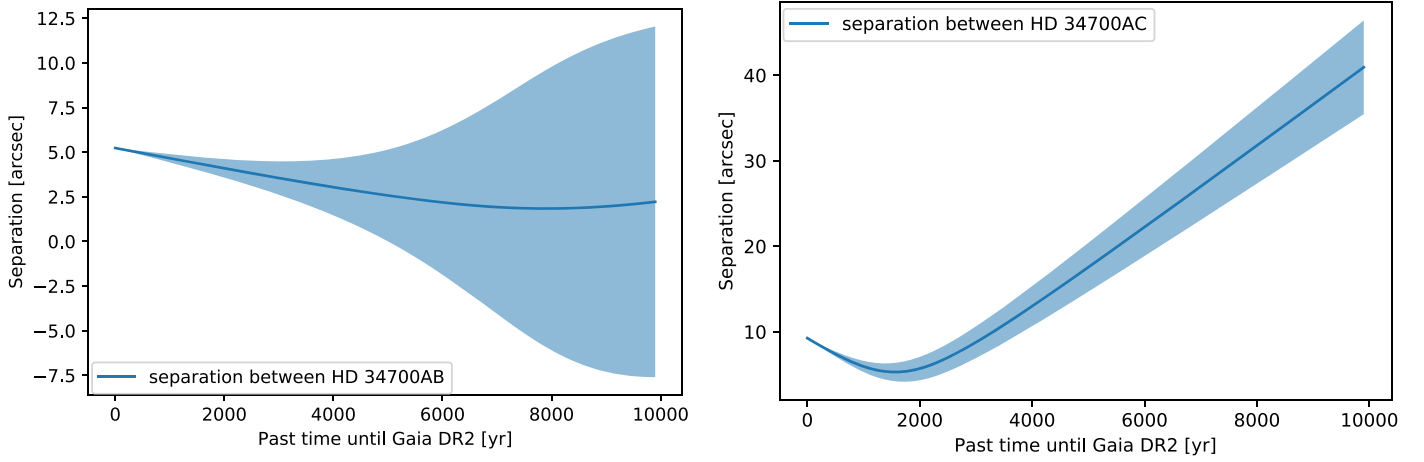
#### Errors of Separation between HD 34700 AB and AC

The error of separation is estimated according to the law of propagation

$$\sigma_r = \sqrt{\left(\frac{\partial r}{\partial \Delta R.A._0} \sigma_{\Delta R.A._0}\right)^2 + \left(\frac{\partial r}{\partial \Delta pm_{R.A.}} \sigma_{\Delta pm_{R.A.}}\right)^2 + \left(\frac{\partial r}{\partial \Delta Decl._0} \sigma_{\Delta Decl._0}\right)^2 + \left(\frac{\partial r}{\partial \Delta pm_{Decl.}} \sigma_{\Delta pm_{Decl.}}\right)^2},$$

where  $\sigma_{\Delta R.A._0}$  and other error parameters above are defined as the sum of squares of the Gaia DR2 measurement errors. In particular, coefficients of the proper motion errors  $\left(\frac{\partial r}{\partial \Delta pm_{R.A.}}$  and  $\frac{\partial r}{\partial \Delta pm_{Decl.}}\right)$  are expressed as  $\frac{\partial r}{\partial \Delta pm_C} = -\frac{t(\Delta C_0 - \Delta pm_C \times t)}{r}$ , where C is R.A. or decl., and have an order of  $t$ . Therefore the errors of the separation increase according to  $t$  if we include the measurement errors of the proper motions (see Figure B1 for the plot with error bars including the proper motion errors).





**Figure B1.** As Figure 12 with both measurement errors of the coordinates and the proper motions. The solid line corresponds to the separation without errors and the shaded area corresponds to the errors.

**Table C1**  
Best-fit Parameters and Errors Obtained from the Fitting of the Gas Infall Model

Parameters	S1a	S1b	S2	S3	S4	S5	S6
Best fit							
$a$ (mas)	45.7	706	290	677	$1.27 \times 10^3$	62.0	876
$b$ (rad)	-0.0472	-0.584	-0.195	-0.588	-0.737	-0.0997	-0.727
$i$ (rad)	-1.54	-1.01	-1.45	-1.15	-1.26	-1.46	-1.11
$\Omega$ (rad)	-1.43	-2.15	-1.54	-0.782	0.331	1.95	1.70
Standard error							
$a$ (mas)	$2.85 \times 10^3$	$1.34 \times 10^3$	$3.26 \times 10^3$	$1.04 \times 10^3$	313	$8.78 \times 10^3$	140
$b$ (rad)	2.96	0.732	2.17	0.764	0.222	13.9	0.0970
$i$ (rad)	1.78	1.18	1.36	0.624	0.0404	16.2	0.0272
$\Omega$ (rad)	0.0939	0.998	0.378	0.627	0.103	1.81	0.119

## Appendix C

### Fitting of Spirals by a Gas Infall Model

Infall of the envelope gas follows a parabolic orbit (see Cassen & Moosman 1981), which is written as



$$r' = \frac{a}{1 - \cos(\theta' - b)},$$

in the coordinates of the orbital plane ( $r'$ ,  $\theta'$ ), where  $a$  and  $b$  are parameters characterizing the orbit. The inclination  $i$  and the position angle  $\Omega$  of the orbital plane are also parameters of the orbit. We fit the observed spirals with the parabolic orbit by assuming that (1) spirals are located foreground and (2) spirals can extend inward from the ring and they may not be detected in the CHARIS image. We summarize the best-fit parameters and the standard errors in Table C1. The errors depend on the traced peaks and the ADI+SDI reduction.

### ORCID iDs

Taichi Uyama <https://orcid.org/0000-0002-6879-3030>  
 Thayne Currie <https://orcid.org/0000-0002-7405-3119>  
 Valentin Christiaens <https://orcid.org/0000-0002-0101-8814>  
 Jaehan Bae <https://orcid.org/0000-0001-7258-770X>

Sanemichi Z. Takahashi <https://orcid.org/0000-0003-3038-364X>  
 Ryo Tazaki <https://orcid.org/0000-0003-1451-6836>  
 Marie Ygouf <https://orcid.org/0000-0001-7591-2731>  
 Jeremy N. Kasdin <https://orcid.org/0000-0002-6963-7486>  
 Tyler Groff <https://orcid.org/0000-0001-5978-3247>  
 Timothy D. Brandt <https://orcid.org/0000-0003-2630-8073>  
 Jeffrey Chilcote <https://orcid.org/0000-0001-6305-7272>  
 Michael W. McElwain <https://orcid.org/0000-0003-0241-8956>  
 Olivier Guyon <https://orcid.org/0000-0002-1097-9908>  
 Julien Lozi <https://orcid.org/0000-0002-3047-1845>  
 Nemanja Jovanovic <https://orcid.org/0000-0001-5213-6207>  
 Frantz Martinache <https://orcid.org/0000-0003-1180-4138>  
 Tomoyuki Kudo <https://orcid.org/0000-0002-9294-1793>  
 Motohide Tamura <https://orcid.org/0000-0002-6510-0681>  
 Eiji Akiyama <https://orcid.org/0000-0002-5082-8880>  
 Charles A. Beichman <https://orcid.org/0000-0002-5627-5471>  
 Carol A. Grady <https://orcid.org/0000-0001-5440-1879>  
 Gillian R. Knapp <https://orcid.org/0000-0002-9259-1164>  
 Jungmi Kwon <https://orcid.org/0000-0003-2815-7774>  
 Michael Sitko <https://orcid.org/0000-0003-1799-1755>  
 Michihiro Takami <https://orcid.org/0000-0001-9248-7546>  
 Kevin R. Wagner <https://orcid.org/0000-0002-4309-6343>

John P. Wisniewski  <https://orcid.org/0000-0001-9209-1808>  
 Yi Yang  <https://orcid.org/0000-0002-9024-4150>

## References

- Andrews, S. M., Huang, J., Pérez, L. M., et al. 2018, *ApJL*, **869**, L41  
 Astropy Collaboration, Price-Whelan, A. M., Sipőcz, B. M., et al. 2018, *AJ*, **156**, 123  
 Astropy Collaboration, Robitaille, T. P., Tollerud, E. J., et al. 2013, *A&A*, **558**, A33  
 Avenhaus, H., Quanz, S. P., Garufi, A., et al. 2018, *ApJ*, **863**, 44  
 Avenhaus, H., Quanz, S. P., Schmid, H. M., et al. 2014, *ApJ*, **781**, 87  
 Bae, J., & Zhu, Z. 2018, *ApJ*, **859**, 119  
 Baraffe, I., Chabrier, G., Barman, T. S., Allard, F., & Hauschildt, P. H. 2003, *A&A*, **402**, 701  
 Benisty, M., Stolker, T., Pohl, A., et al. 2017, *A&A*, **597**, A42  
 Bertrang, G. H. M., Avenhaus, H., Casassus, S., et al. 2018, *MNRAS*, **474**, 5105  
 Bonnefoy, M., Chauvin, G., Lagrange, A. M., et al. 2014, *A&A*, **562**, A127  
 Bowler, B. P. 2016, *PASP*, **128**, 102001  
 Brandt, T. D., Rizzo, M., Groff, T., et al. 2017, *JATIS*, **3**, 048002  
 Brauer, R., Pantin, E., di Folco, E., et al. 2019, *A&A*, **628**, A88  
 Canovas, H., Hardy, A., Zurlo, A., et al. 2017, *A&A*, **598**, A43  
 Casassus, S., Avenhaus, H., Pérez, S., et al. 2018, *MNRAS*, **477**, 5104  
 Cassen, P., & Moosman, A. 1981, *Icar*, **48**, 353  
 Castellì, F., & Kurucz, R. L. 2003, in IAU Symp. 210, Modelling of Stellar Atmospheres, ed. N. Piskunov, W. W. Weiss, & D. F. Gray (San Francisco, CA: ASP), A20  
 Christiaens, V., Casassus, S., Perez, S., van der Plas, G., & Ménard, F. 2014, *ApJL*, **785**, L12  
 Cuello, N., Dipierro, G., Mentiplay, D., et al. 2019, *MNRAS*, **483**, 4114  
 Cuello, N., Louvet, F., Mentiplay, D., et al. 2020, *MNRAS*, **491**, 504  
 Currie, T., Brandt, T. D., Uyama, T., et al. 2018, *AJ*, **156**, 291  
 Currie, T., Burrows, A., Itoh, Y., et al. 2011, *ApJ*, **729**, 128  
 Currie, T., Burrows, A., Madhusudhan, N., et al. 2013, *ApJ*, **776**, 15  
 Currie, T., Cloutier, R., Brittain, S., et al. 2015, *ApJL*, **814**, L27  
 Currie, T., Debes, J., Rodigas, T. J., et al. 2012, *ApJL*, **760**, L32  
 Currie, T., Marois, C., Cieza, L., et al. 2019, *ApJL*, **877**, L3  
 Cutri, R. M., Skrutskie, M. F., van Dyk, S., et al. 2003, *yCat*, II/246  
 Dai, F., Facchini, S., Clarke, C. J., & Haworth, T. J. 2015, *MNRAS*, **449**, 1996  
 Debes, J. H., Poteet, C. A., Jang-Condell, H., et al. 2017, *ApJ*, **835**, 205  
 Demidova, T. V., & Shevchenko, I. I. 2015, *ApJ*, **805**, 38  
 Dodson-Robinson, S. E., & Salyk, C. 2011, *ApJ*, **738**, 131  
 Dong, R., Fung, J., & Chiang, E. 2016, *ApJ*, **826**, 75  
 Dong, R., Liu, S.-y., Eisner, J., et al. 2018b, *ApJ*, **860**, 124  
 Dong, R., Najita, J. R., & Brittain, S. 2018a, *ApJ*, **862**, 103  
 Dong, R., Zhu, Z., Rafikov, R. R., & Stone, J. M. 2015, *ApJL*, **809**, L5  
 Dullemond, C. P., Kuffmeier, M., Goicovic, F., et al. 2019, *A&A*, **628**, A20  
 Fukagawa, M., Hayashi, M., Tamura, M., et al. 2004, *ApJL*, **605**, L53  
 Fukagawa, M., Tamura, M., Itoh, Y., et al. 2006, *ApJL*, **636**, L153  
 Gaia Collaboration, Brown, A. G. A., Vallenari, A., et al. 2018, *A&A*, **616**, A1  
 Grady, C. A., Muto, T., Hashimoto, J., et al. 2013, *ApJ*, **762**, 48  
 Haffert, S. Y., Bohn, A. J., de Boer, J., et al. 2019, *NatAs*, **3**, 749  
 Hammel, B., & Sullivan-Molina, N. 2020, bdhammel/least-squares-ellipse-fitting: v2.0.0, Zenodo, doi:10.5281/zenodo.3723294  
 Hashimoto, J., Tamura, M., Muto, T., et al. 2011, *ApJL*, **729**, L17  
 Itoh, Y., Oasa, Y., Kudo, T., et al. 2014, *RAA*, **14**, 1438  
 Itoh, Y., Tamura, M., Hayashi, S. S., et al. 2002, *PASJ*, **54**, 963  
 Jovanovic, N., Guyon, O., Martinache, F., et al. 2015, *ApJL*, **813**, L24  
 Keppler, M., Benisty, M., Müller, A., et al. 2018, *A&A*, **617**, A44  
 Keppler, M., Penzlin, A., Benisty, M., et al. 2020, *A&A*, **639**, A62  
 Krist, J. E., Stapelfeldt, K. R., & Watson, A. M. 2002, *ApJ*, **570**, 785  
 Lafrenière, D., Marois, C., Doyon, R., & Barman, T. 2009, *ApJL*, **694**, L148  
 Lafrenière, D., Marois, C., Doyon, R., Nadeau, D., & Artigau, É. 2007, *ApJ*, **660**, 770  
 Laws, A. S. E., Harries, T. J., Setterholm, B. R., et al. 2020, *ApJ*, **888**, 7  
 Marino, S., Perez, S., & Casassus, S. 2015, *ApJL*, **798**, L44  
 Marois, C., Lafrenière, D., Doyon, R., Macintosh, B., & Nadeau, D. 2006, *ApJ*, **641**, 556  
 Mawet, D., Milli, J., Wahhaj, Z., et al. 2014, *ApJ*, **792**, 97  
 Ménard, F., Cuello, N., Ginski, C., et al. 2020, *A&A*, **639**, L1  
 Min, M., Dullemond, C. P., Dominik, C., de Koter, A., & Hovenier, J. W. 2009, *A&A*, **497**, 155  
 Monnier, J. D., Harries, T. J., Bae, J., et al. 2019, *ApJ*, **872**, 122  
 Montesinos, M., & Cuello, N. 2018, *MNRAS*, **475**, L35  
 Montesinos, M., Perez, S., Casassus, S., et al. 2016, *ApJL*, **823**, L8  
 Mulders, G. D., Dominik, C., & Min, M. 2010, *A&A*, **512**, A11  
 Mulders, G. D., Min, M., Dominik, C., Debes, J. H., & Schneider, G. 2013, *A&A*, **549**, A112  
 Muto, T., Grady, C. A., Hashimoto, J., et al. 2012, *ApJL*, **748**, L22  
 Nielsen, E. L., de Rosa, R. J., Macintosh, B., et al. 2019, *AJ*, **158**, 13  
 Pérez, L. M., Carpenter, J. M., Andrews, S. M., et al. 2016, *Sci*, **353**, 1519  
 Price, D. J., Cuello, N., Pinte, C., et al. 2018, *MNRAS*, **477**, 1270  
 Quanz, S. P., Amara, A., Meyer, M. R., et al. 2013, *ApJL*, **766**, L1  
 Quillen, A. C. 2006, *ApJ*, **640**, 1078  
 Reggiani, M., Christiaens, V., Absil, O., et al. 2018, *A&A*, **611**, A74  
 Rice, W. K. M., Armitage, P. J., Bate, M. R., & Bonnell, I. A. 2003, *MNRAS*, **339**, 1025  
 Rich, E. A., Wisniewski, J. P., Currie, T., et al. 2019, *ApJ*, **875**, 38  
 Rodriguez, J. E., Loomis, R., Cabrit, S., et al. 2018, *ApJ*, **859**, 150  
 Sahoo, A., Guyon, O., Lozi, J., et al. 2020, *AJ*, **159**, 250  
 Soummer, R., Pueyo, L., & Larkin, J. 2012, *ApJL*, **755**, L28  
 Spiegel, D. S., & Burrows, A. 2012, *ApJ*, **745**, 174  
 Sterzik, M. F., Melo, C. H. F., Tokovinin, A. A., & van der Bliik, N. 2005, *A&A*, **434**, 671  
 Stolker, T., Dominik, C., Min, M., et al. 2016, *A&A*, **596**, A70  
 Stolker, T., Sitko, M., Lazareff, B., et al. 2017, *ApJ*, **849**, 143  
 Takami, M., Karr, J. L., Hashimoto, J., et al. 2013, *ApJ*, **772**, 145  
 Tang, Y.-W., Guilloteau, S., Dutrey, A., et al. 2017, *ApJ*, **840**, 32  
 Tang, Y. W., Guilloteau, S., Piétu, V., et al. 2012, *A&A*, **547**, A84  
 Thalmann, C., Mulders, G. D., Hodapp, K., et al. 2014, *A&A*, **566**, A51  
 Torres, G. 2004, *AJ*, **127**, 1187  
 Uyama, T., Hashimoto, J., Muto, T., et al. 2018, *AJ*, **156**, 63  
 Uyama, T., Muto, T., Mawet, D., et al. 2020, *AJ*, **159**, 118  
 Vigan, A., Gry, C., Salter, G., et al. 2015, *MNRAS*, **454**, 129  
 Wagner, K., Apai, D., Kasper, M., & Robberto, M. 2015, *ApJL*, **813**, L2  
 Wagner, K., Follete, K. B., Close, L. M., et al. 2018, *ApJL*, **863**, L8  
 Wisniewski, J. P., Clampin, M., Grady, C. A., et al. 2008, *ApJ*, **682**, 548  
 Ygouf, M., Patel, R., Debes, J., et al. 2019, AAS Meeting Abstracts, **233**, 436.02  
 Zhu, Z., Dong, R., Stone, J. M., & Rafikov, R. R. 2015, *ApJ*, **813**, 88  
 Zhu, Z., Nelson, R. P., Hartmann, L., Espaillat, C., & Calvet, N. 2011, *ApJ*, **729**, 47